Journal of the Iowa Academy of Science: JIAS

Volume 121 | Number 1-4 Article 3

2014

Synchronous Rotation in the Eclipsing Binary 68 Herculis Inferred from Doppler Shifts in its Spectrum and Light Curve Modeling

Kenneth W. McLaughlin
Loras College

Janak Panthi
Loras College

Jour. Iowa Acad. Sci. 121(1-4):5–15, 2014

Synchronous Rotation in the Eclipsing Binary 68 Herculis Inferred from Doppler Shifts in its Spectrum and Light Curve Modeling

KENNETH W. MCLAUGHLIN* and JANAK PANTHI

Science Hall, Room 123, Loras College, Dubuque, Iowa

Our differential photometry of the eclipsing binary 68 Herculis through V- and R-filters shows periodic minima consistent with a previously established period. As a function of its orbital motion, we report spectra over a limited wavelength range encompassing H-alpha 656.3 nm and helium 667.8 nm lines. Doppler shifts of both stars were resolved in H-alpha, while only the more massive star rendered the helium line with Doppler shifts that agree with the radial velocity we derive for it from the H-alpha profile. Sinusoidal curve-fits to the orbital dependence of the radial velocities imply circular orbits for both components, with amplitudes indicating a mass ratio for the two stars in agreement with published values. A subtle Doppler shift associated with stellar rotation is evident in the radial velocity of the primary component as its eclipse commences; modeling indicates this rotation is synchronous with the orbital revolution, an expected tidal effect of near-contact binary systems.

INDEX DESCRIPTORS: eclipsing binary, light curve, orbital parameters, Doppler shifts.

INTRODUCTION

Eclipsing binaries allow one of the most direct assessments of the key parameter dictating stellar evolution: mass. Previous studies of 68 Herculis, which we abbreviate as 68Her, have recognized an eclipsing binary model for its variability with a well-established period of just over two days (Henden and Kaitchuck 1982, Kreiner 2004). Repeated monitoring is warranted as short orbital periods require tight orbital distances that can promote the transfer of material between the two stars, altering their evolution – although the evidence for this in 68Her has been contradictory in recent investigations (Soderhjelm 1978, Hilditch 2005, Kolbas et al. 2014). 68Her varies in visible magnitude from 4.7 to 5.4, and because spectral studies (Olson 1968) assign the components as early and late O-type stars, modest telescopes can explore prominent hydrogen and helium lines.

We present photometry of 68Her through V- and R-filters, both of which show repeating minima consistent with the established period. We also present spectroscopy over a 75 nm range encompassing H-alpha 656.3 nm and the helium 667.8 nm line. Doppler shifts of both stars were resolved in the H-alpha absorption, while only the more massive star displayed significant helium absorption, with Doppler-shifts that agree with the radial velocity we derive for it from the H-alpha profile. Sinusoidal curve-fits to the orbital dependence of the radial velocities indicate circular orbits for the two stars whereby the amplitudes of these fits specify the ratio of the stellar masses as 3.16 with an uncertainty of 3.7%, in agreement with previous assessments (Kovachev and Seggewiss 1975, Hilditch 2005).

We synthesized light curves in agreement with our photometry using values for the orbital inclination as well as stellar temperatures and diameters that conform with published values (Rovithis-Livaniou and Rovithis 1985, van der Veen 1985). Our results agree with those of Kovachev and Seggewiss (1975) and Hilditch (2005) that this binary system has not changed significantly since the early determinations by Sterne (1941) and Smith (1945).

A subtle Doppler shift associated with stellar rotation is evident in the radial velocity of the primary component as its eclipse commences; our modeling suggests this rotation is synchronous with the orbital revolution, an expected tidal effect of near-contact binary systems. This rotational influence has been observed in many eclipsing binaries since the explanation given by Rossiter (1924), and was evident in the radial velocities for 68Her reported by Smith (1945: fig. 1). Three decades later, Kovachev and Seggewiss (1975) noted that the Rossiter effect was ''less noticeable'' in their radial velocities, which stimulated our investigation.

METHODS

Our roll-off roof observatory houses three telescopes on concrete piers. Although moderately shielded by trees and not in proximity to obtrusive lighting, it is located on an urban campus at latitude 42°30′15″, longitude 90°40′40″, and elevation 750 ft above sea level.

We used a commercially available cooled charge-coupled device (CCD) camera: SBIG ST8 with 9-μm square pixels (Santa Barbara Instrument Group 2015). Preceding the camera was a V-filter (Munari and Moretti 2012) that only transmitted light within the bandwidth of approximately 500 to 600 nm. This assembly was attached to a commercially available fork-mounted Schmidt–Cassegrain telescope (SCT): Meade LX200 f/10 with a 3.556 m focal length. No changes were made to this set-up for 12 weeks once photometry began in early June 2013; a similar campaign commenced the following June with the same camera and SCT now equipped with a filter-wheel, allowing both V- and

* Corresponding author: kenneth.mclaughlin@loras.edu

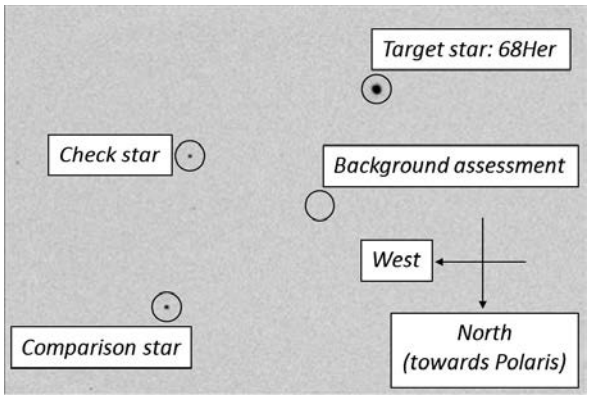

Fig. 1. Photonegative of a calibrated 8.9 × 13.3 arc-minute image designating the target, comparison, and check stars along with a typical area used for background assessment.

R-filtered images whereby the latter filter only transmitted light of approximately 570–700 nm.

Raw images, with exposures limited to maintain the linear response of the CCD, were calibrated by dark-count subtraction and flat-fielded by sky flats (Berry and Burnell 2005). Figure 1 illustrates how we assessed stellar brightness by summing the pixel values within an area around each star, followed by subtracting a similar assessment for sky background. The pixel summations were accomplished with both the software provided by the camera manufacturer and that accompanying Berry and Burnell (2005); while the former uses square areas and the latter uses circular areas with an annulus around each star for background assessment, we found no difference in the differential photometry between the softwares.

Differential photometry factors out the instrumental efficiency by taking the ratio of the brightness for 68Her and a "Comparison" star in the same field of view; this ratio is equivalent to the difference in stellar magnitudes, as the latter is based on a logarithmic scale. A similar assessment between the "Comparison" and a "Check" star indicated only statistical variance as shown in Fig. 2, which plots our V-filtered differential magnitudes as a function of the orbital phase computed as a decimal fraction of the orbital period T_{period} = 2.05102655 days:

$$Phase = \frac{(Observation\ Julian\ Date - preceding\ primary\ minimum)}{T_{period}} \quad (1)$$

The Julian Date of the preceding primary eclipse was specified by the ephemeris given by Kreiner (2004). Our photometry encompassed 220 cycles, with 80 cycles of data coverage folded into a data set with phase between 0 and 1 – although we repeat this on both sides of this range in the light curve of Fig. 2 to aid visualizing the primary eclipse.

We used a commercially available spectrometer SBIG SGS with a cooled-CCD ST-7 detector with 9-μm pixels, producing

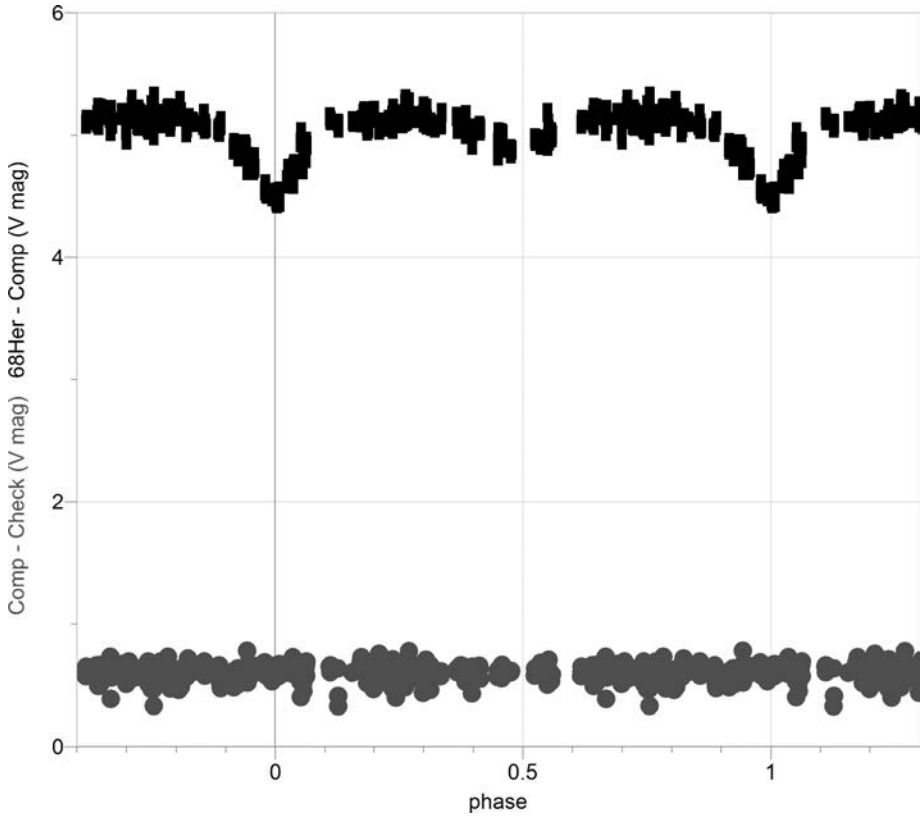

Fig. 2. The light-curve of our V-filter magnitudes as a function of orbital phase: black boxes denote the magnitude differences between 68Her and Comparison star; gray circles denote the magnitude differences between Check and Comparison stars.

Fig. 3. Raw spectra following dark-count subtraction for 68Her (phase 0.737); Neon gas-discharge (for wavelength calibration); and Vega (for flux calibration).

a dispersion of 0.107 nm/pixel (Holmes 2009). This was attached to an equatorial-mounted SCT: Meade LX850 f/8 with a 2.845 m focal length. No changes were made to this set-up for the 8 weeks for which spectra were acquired beginning in early June 2013; a similar campaign began in June 2014. Exposures for 68Her spectra required 20 min for an acceptable signal-to-noise ratio of approximately 20:1, while those for Vega, used for flux calibration, were accomplished in only 10 s. Spectra were acquired with the target within 1 h of transiting the meridian – for example, from 2300 to 0100 on the last evening of June, when 68Her is in opposition to the Sun. This restricted observing window minimized the radial component toward 68Her due to the rotational and orbital motion of Earth; therefore, we have made no corrections to our spectra due to Earth's motion.

Following dark-count subtraction, a raw spectrum came from summing eight vertical pixels encompassing the spectra shown in Fig. 3, followed by subtracting a similar assessment for the average of the sky background above and below the stellar spectrum. With no movement of the telescope but with the observatory roof partially closed to block starlight, wavelength

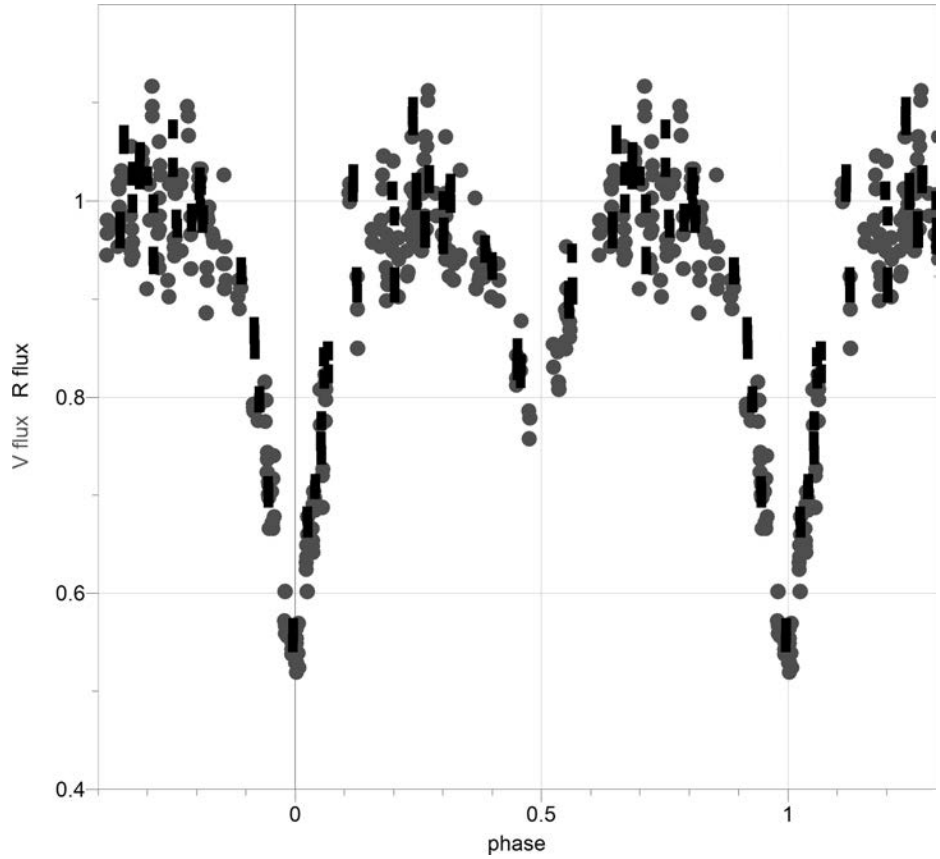

Fig. 4. Overlain V- and R-filter light curves in terms of linear flux as a decimal fraction of the flux when the system is not eclipsed: black boxes denote R-filter; gray circles denote V-filter.

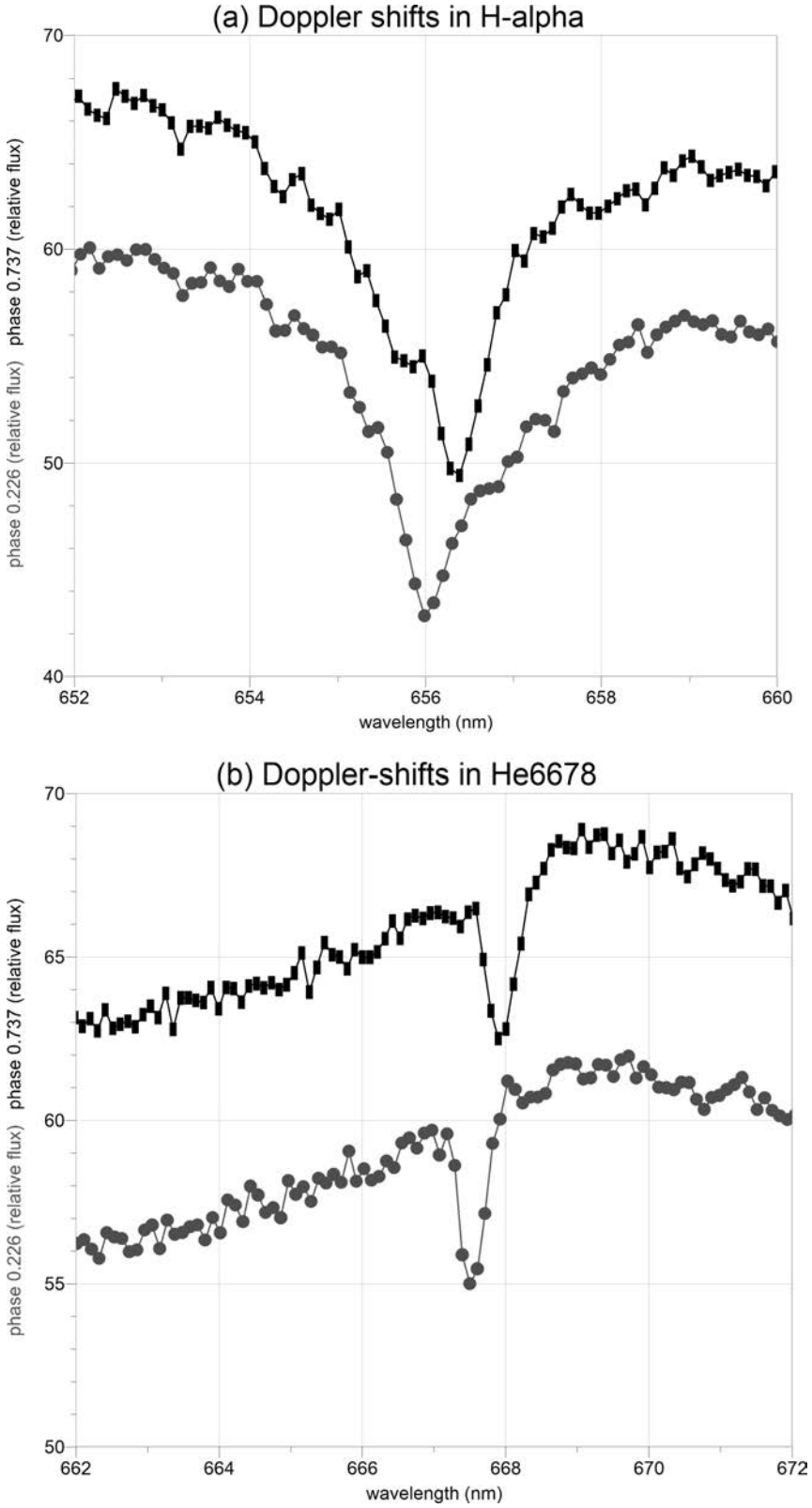

Fig. 5. Doppler shifts in (a) H-alpha and (b) He6678: black boxes denote a spectrum acquired with orbital phase 0.737 shifted vertically upwards 7 percentage points for clarity; gray circles denote a phase 0.226 spectrum. The vertical axis is the percentage fraction of an arbitrarily chosen flux value; the individual pixel values are connected merely as a visual aid.

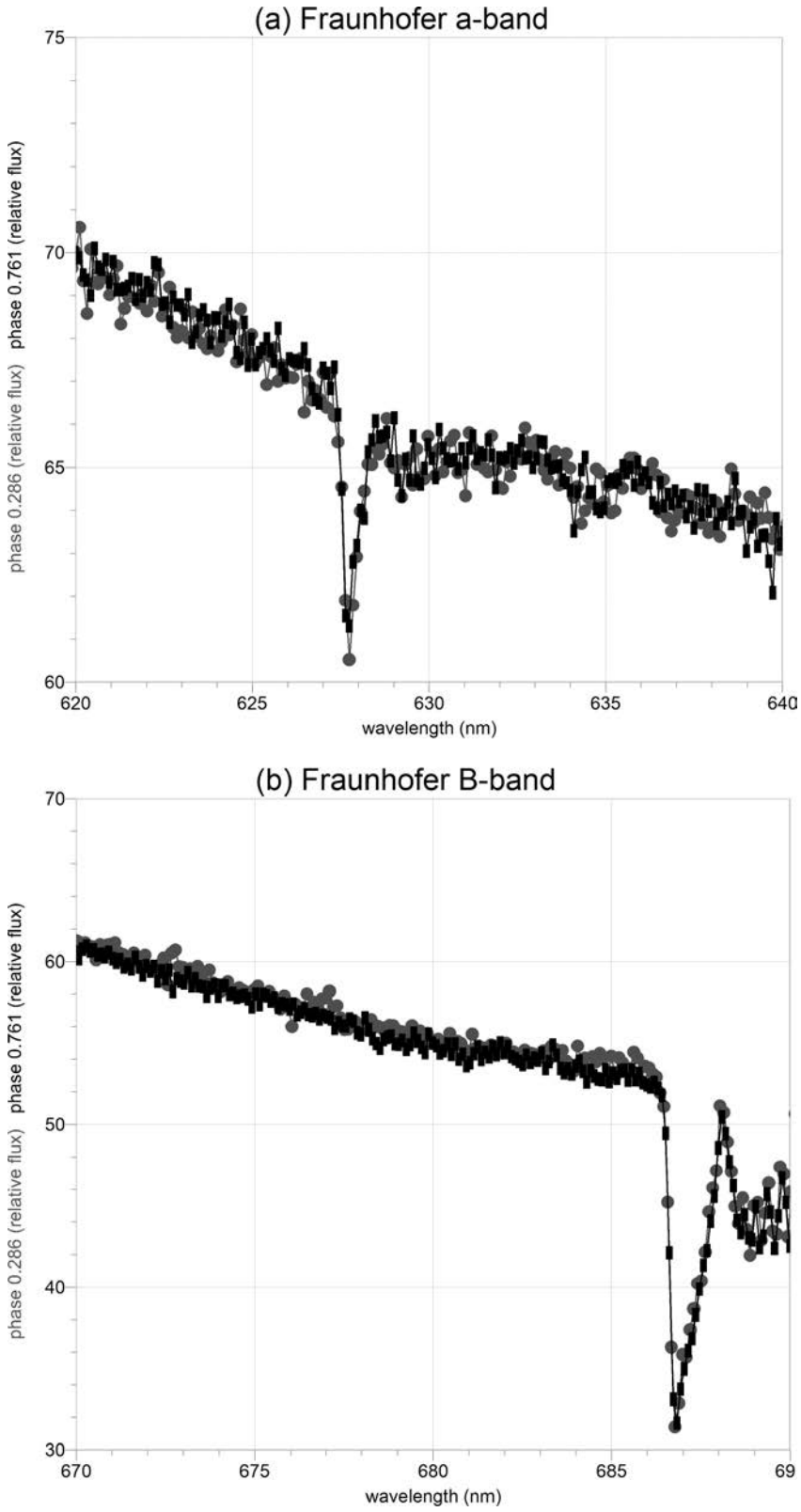

Fig. 6. Reproducibility in the telluric lines of atmospheric oxygen: (a) the Fraunhofer a-band near 627.7 nm and (b) B-band near 687 nm: black boxes denote a spectrum acquired with orbital phase 0.761; gray circles denote a phase 0.286 spectrum. The individual pixel values are connected merely as a visual aid.

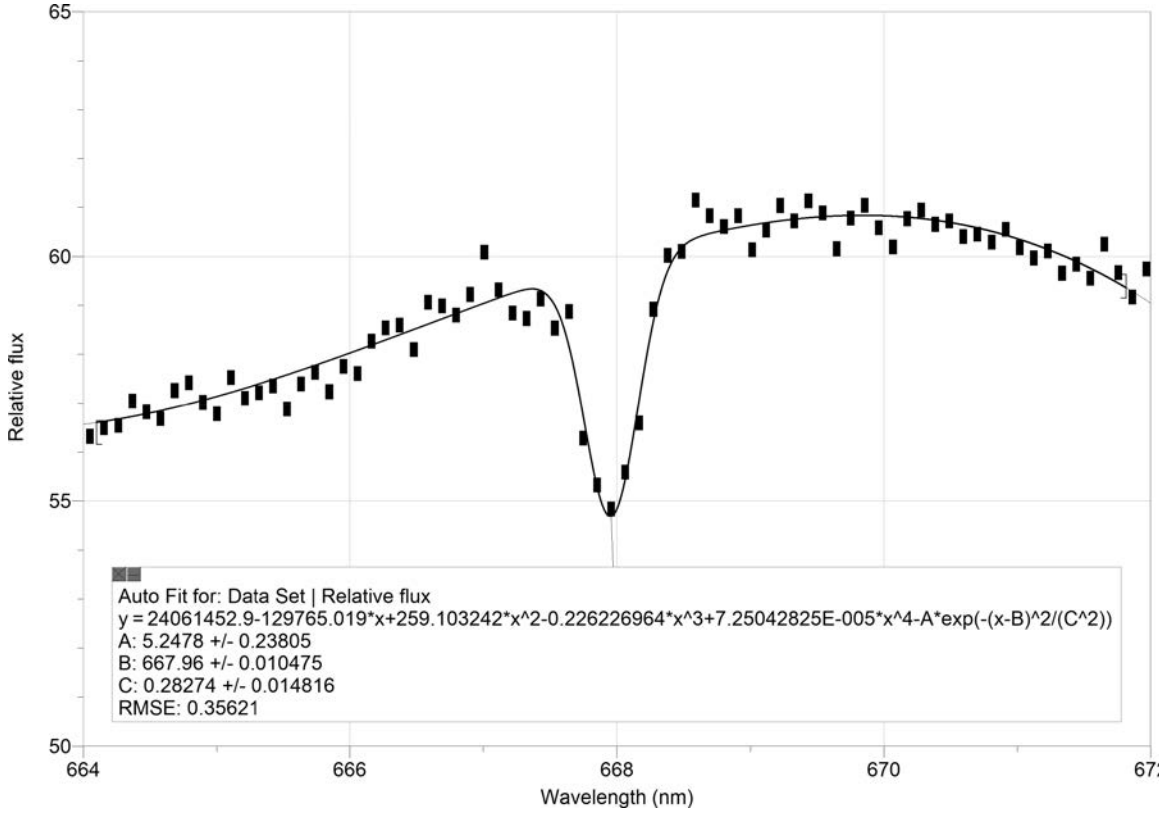

Fig. 7. Curve-fit to He6678 absorption when the system is not eclipsed (phase 0.761); the black boxes denote the individual pixel values with a solid line denoting the curve fit to the continuum with a Gaussian absorption profile.

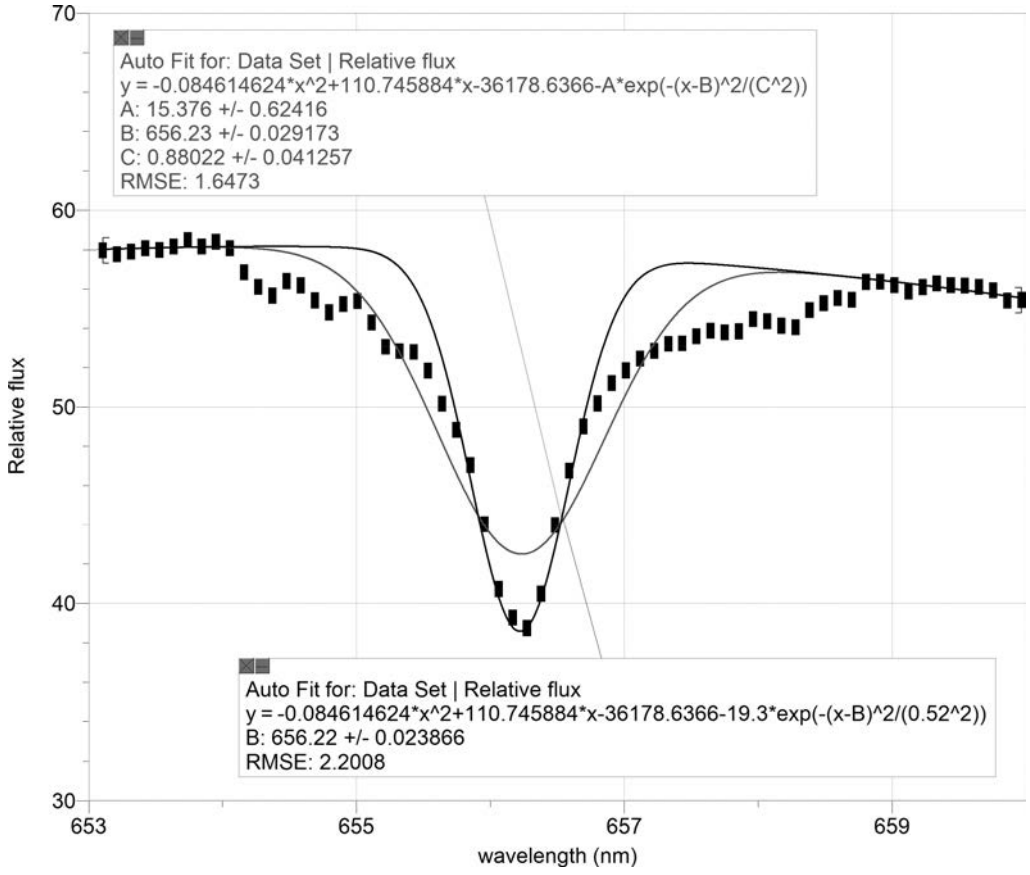

Fig. 8. Gaussian curve-fits of the H-alpha absorption during the secondary eclipse, when the primary component dominates the spectrum (phase 0.525).

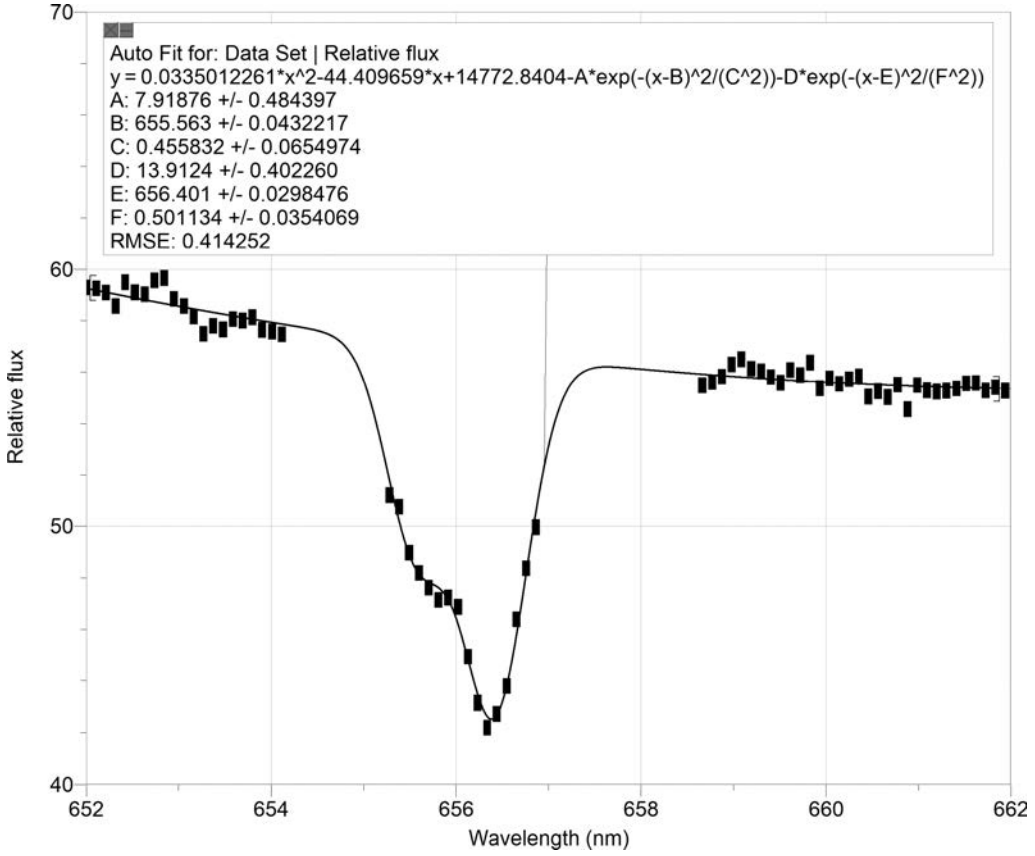

Fig. 9. Gaussian curve-fit to H-alpha absorption when the system is not eclipsed (phase 0.761).

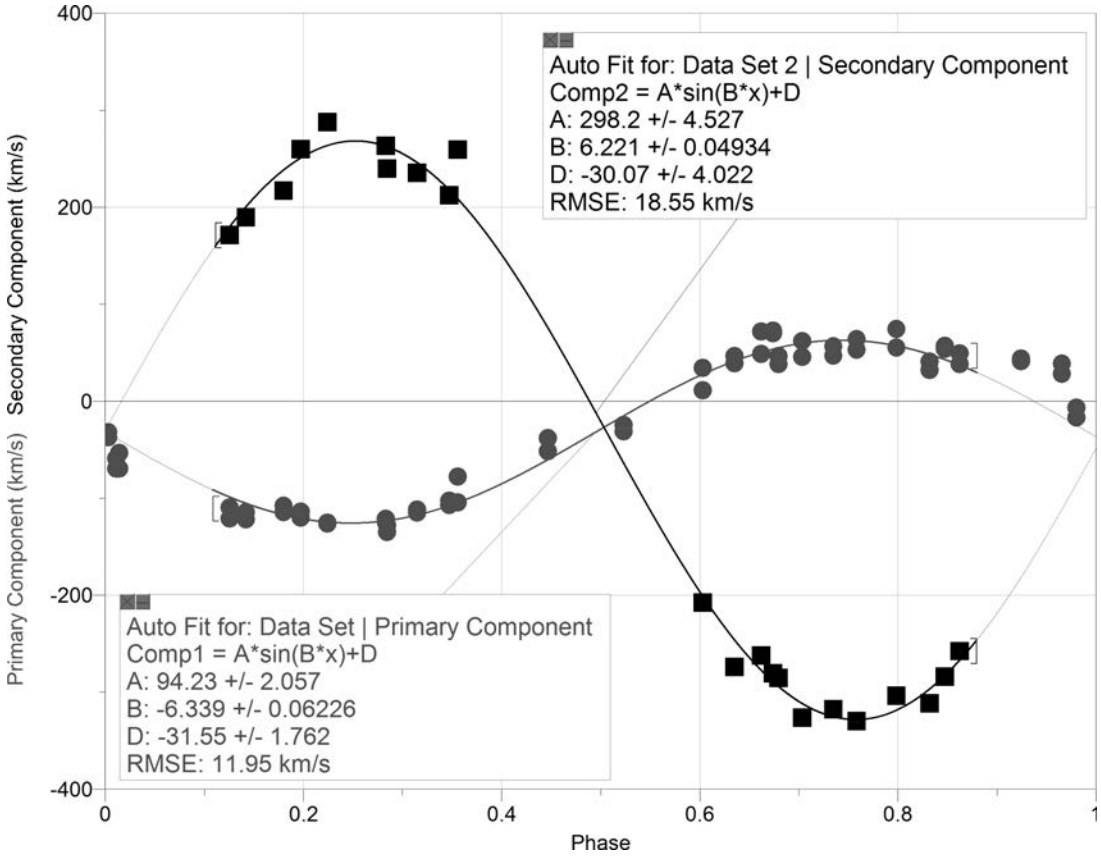

Fig. 10. Sinusoidal curve-fits to the radial velocities: black boxes denote the secondary component; gray circles denote the primary component.

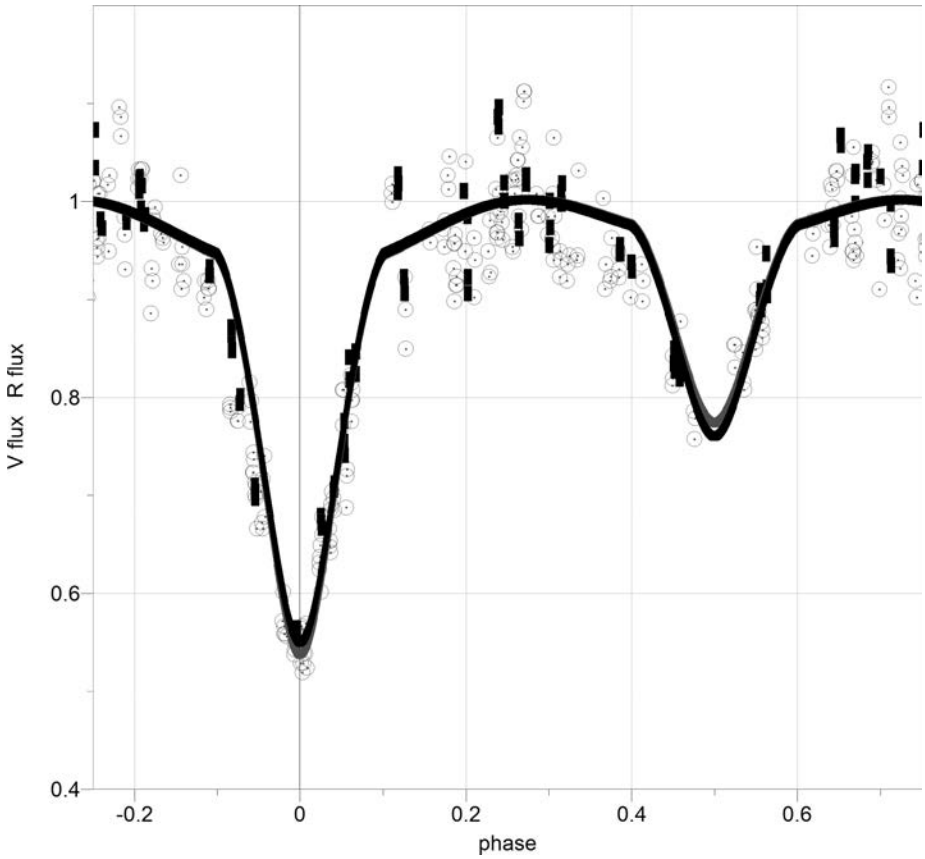

Fig. 11. Synthesized light-curves: the black line denotes the R-filter light-curve with black boxes denoting the R-filter data; the gray line denotes the V-filter light-curve with gray circles denoting the V-filter data.

calibration was accomplished with a neon gas discharge held 1 m above the telescope immediately following the acquisition of stellar spectra; the neon spectrum came from summing the same central eight vertical pixels used with the stellar spectra. We fit Gaussian profiles to the 13 strongest neon lines from 614.306 to 671.704 nm (Kramida et al. 2014), allowing a sub-pixel location to be assigned to their centerlines; linear regression between these centerlines and their published wavelengths confirmed the H-alpha 656.285 nm and helium 667.815 nm lines to within 0.02 nm for hydrogen and helium gas discharges similarly held above the telescope.

Following wavelength calibration, pixel variation in signal-sensitivity was accounted for by acquiring the spectrum of the nearby star Vega. Removing absorption lines in order to use only the continuum portion of the spectra, the ratio between its published spectrum (Spectrophotometric Standard Stars 2013) and our Vega spectrum generated an Instrumental Response Factor (IRF) that we used to calibrate the 68Her spectral flux. These IRFs were well replicated throughout our campaign and agreed with the spectral response of the quantum efficiency reported for the CCD detector over our range of interest: decreasing from approximately 35% at 600 nm to 28% at 700 nm (Eastman Kodak 2013).

Table 1. Parameters[a] for synthesizing 68Her light-curves and associated radial velocities using the modeling program Binary Maker 3 (Bradstreet 2005).

	Primary Component	Secondary Component
Surface temperatures (K)	19200 ± 900	12500 ± 800
Fractional stellar radii[b]	0.338 ± 0.015	0.292 ± 0.013

[a]The eccentricity had an optimal value of 0 with an upper limit of 0.02, and the mass ratio was set at the value from our radial velocity determination of 3.16 ± 3.7% with an orbital inclination of 80.7 ± 0.9°, while standard linear limb-darkening coefficients, gravity-brightening exponents and albedo fractions for the "radiative" surfaces for both stars were adopted (Bradstreet 2005)

[b]The fractional stellar radii are the "back" radii, which have less tidal distortion than the "front" side facing the other component, and these are "fractional" values because they are relative to the Kepler law parameter of the average orbital distance, which is the sum of the two orbital radii for the case of circular orbits

RESULTS

We can compare our V- and R-filter photometry by converting from the differential magnitudes Δm to a linear flux scale (Carroll and Ostlie 2007) using:

$$relative\ flux = 100^{\Delta m/5} \quad (2)$$

Figure 4 overlays the V- and R-filter light curves as a decimal fraction of the average flux when the system is not eclipsed. Although Hilditch (2005) reviews the evidence for variability in 68Her due to pulsations and gas streams, the poor statistics when 68Her is brightest is a shortcoming of our differential photometry, as its greater flux limits the exposure such that the statistical noise in the comparison star was not sufficiently reduced; nevertheless, the primary minima affirms the ephemeris given by Kreiner (2004).

Figure 5 shows the reinforcing Doppler shifts of the primary component in both H- alpha and He6678, while the secondary component is observed in only the former. Figure 6 reinforces these shifts as due to the orbital motion of 68Her, as the telluric lines of atmospheric oxygen near 627.7 and 687 nm, the Fraunhofer A- and B-bands, were consistently reproduced in our spectra with no shifts.

DISCUSSION

Absorption centerlines were determined by curve-fitting a Gaussian profile on a previously determined fit to the continuum, as Fig. 7 illustrates for the He6678 line. A radial velocity v along the line-of-sight from Earth was associated with the observed centerline $\lambda_{observed}$ of the profile using (Carroll and Ostlie 2007):

$$\frac{^{\lambda}observed - {}^{\lambda}rest}{^{\lambda}rest} = \frac{v}{c} \tag{3}$$

This well-known Doppler effect connects the relative change in the observed wavelength from the laboratory rest value λ_{rest} to the radial velocity along the line of sight relative to the speed of light c. The centerline precision in Fig. 7, $\lambda_{observed} \cong 667.96 \pm 0.01$ nm, is comparable to the confidence we discussed with our wavelength calibration; this centerline precision as well as the fit-parameter for the width of the Gaussian ($\cong 0.3$ nm) was typical for all of our He6678 profile fits.

As Fig. 8 illustrates, curve-fits to the H-alpha absorption were more challenging – even for spectra acquired near the secondary minimum, when the primary component dominates the spectrum. Broad hydrogen profiles can be attributed (Carroll and Ostlie 2007) to variance in optical depth across the stellar atmosphere for the dominating stellar component of hydrogen; early investigators (Smith 1945) often avoided using hydrogen profiling because of this difficulty, though later studies successfully used the Doppler shifts (Kovachev and Seggewiss 1975) and widths (Kovachev and Reinhardt 1975) of hydrogen lines.

Although a simple Gaussian cannot model the entire H-alpha profile, the centerline of the fit is not sensitive to "ignoring the wings" or restricting the Gaussian width to that comparable for the helium line. Figure 8 shows that the innermost region of the absorption can be fit with a centerline indistinguishable from that from a general Gaussian fit. We found similar results when we attempted Lorentzian profiles: an inability to fit the entire profile but insensitivity to the centerline parameter for varying width parameter settings. Thus, we arrived at the following procedure for fitting the H-alpha absorption, as illustrated in Fig. 9: excise the same section of the "wings" of the profile and fit to two Gaussian absorptions, with the dominant profile attributed to the primary star and the less prominent profile attributed to the secondary. Figure 10 supports this procedure, as the radial velocity for the primary component derived from its Doppler shifts in the H-alpha profile agrees with that obtained from the helium line. There are two primary radial velocities for every secondary component velocity except near eclipses, where the secondary profile was not resolved and we only have primary component velocity.

Figure 10 shows that the orbital dependence of the radial velocities is sufficiently sinusoidal to infer circular orbits for the two components, as noted in the previous studies of 68Her we have referenced. The dependence on the inclination angle for these orbits factors out (Carroll and Ostlie 2007) in the ratio of the amplitudes of the sinusoidal fits and yields the ratio of the stellar masses as $3.16 \pm 3.7\%$; our value is slightly higher than previous assessments (Kovachev and Seggewiss 1975, Hilditch 2005) but within 1.6 SD; our blue-shifted values for the center-of-mass motion given by the offsets in Fig. 10 of approximately -30 km s^{-1} similarly agree with all previous assessments, as well as those dating back to the earliest studies of Sterne (1941) and Smith (1945).

We restricted our curve-fit for the primary component in Fig. 10 to avoid the region near the primary eclipse, where there is a systematic discrepancy from the pure sinusoidal predictor; this is the region in which the *rotational* motion of the primary star influences the Doppler shift that is usually integrated across its entire atmosphere when not eclipsed. Modeling this shift

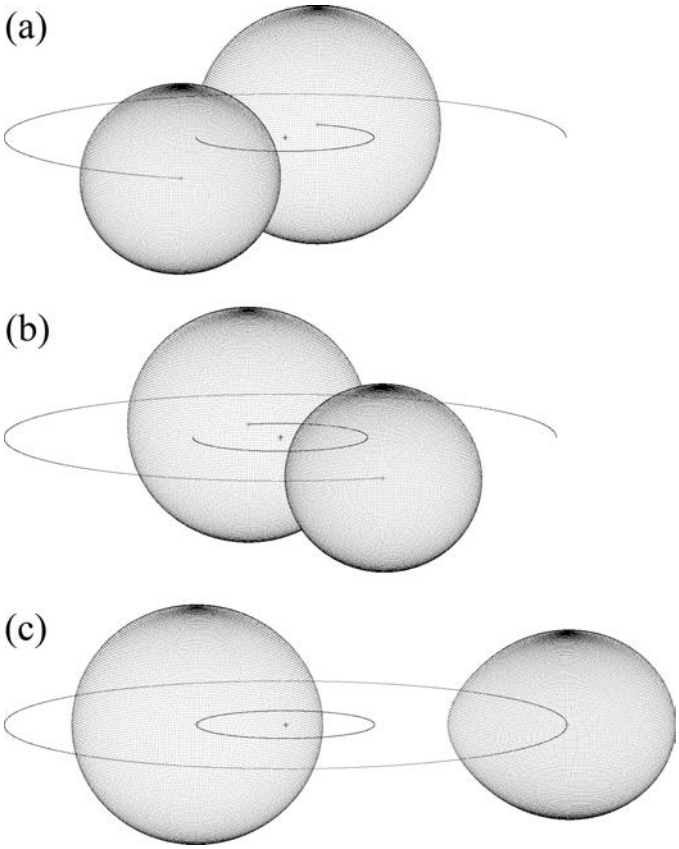

Fig. 12. A scale-model of the stellar and orbital dimensions with: (a) phase 0.94 as the primary eclipse begins; (b) phase 0.06 with the primary component emerging from its eclipse; and (c) phase 0.25. Due to the inclination angle of the orbital plane from our line of sight, the circular orbits of the center of mass for each star shown by the solid line appear oblique.

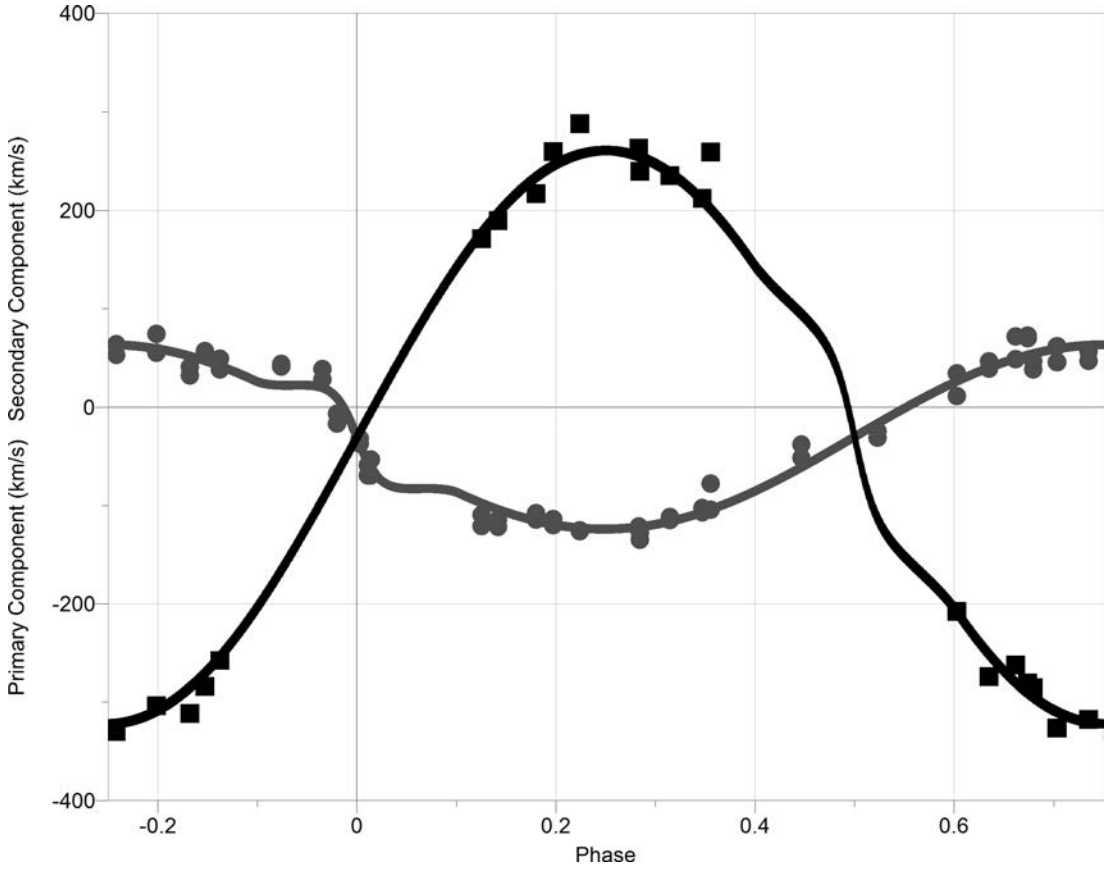

Fig. 13. Synthesized radial velocities: the black line denotes that for the secondary component with black boxes denoting the data; the gray line denotes that for the primary component with gray boxes denoting data.

across an eclipsed portion of the atmosphere will invoke the inclination of the orbit, and to infer that inclination we pursued modeling our light curves.

In addition to the values for orbital inclination as well as stellar temperatures, diameters and mass ratio, synthesizing eclipsing binary light-curves includes the effect of limb-darkening as well as the reflection and tidal distortions important for tight orbital distances (Kallrath and Milone 2009). Using the modeling program Binary Maker 3 (Bradstreet 2005), we synthesized light curves in agreement with our photometry (Fig. 11) using the parameters given in Table 1, where our 1SD uncertainties encompass the range of these values previously reported (Rovithis-Livaniou and Rovithis 1985, van der Veen 1985, Hilditch 2005).

Although the scatter in our photometry limits us from advancing any further restrictions on these parameters, our modest R-filter data coverage of the primary eclipse does agree with the prediction of a modestly greater depth for the V-filter when the hotter star is eclipsed. Similarly, the model predicts a modestly greater depth for the R-filter when the cooler component is eclipsed, although the secondary eclipse was not well sampled with either set of our data and especially not with the R-filter. Our light-curve modeling predicts the scale model of the stellar and orbital dimensions shown in Fig. 12; the tidal distortion and near-filling of the secondary component's Roche lobe (Kallrath and Milone 2009) agree with those found by previous authors (Provoost 1980, van der Veen 1985, Hilditch 2005). Although an early study (Sterne 1941) suggested a small eccentricity of 0.053 $\pm$ 0.014, in order to agree with our photometry and radial velocities, our modeling places an upper limit of 0.02 on the eccentricity of these orbits.

Light curve modeling also predicts the radial velocities. Figure 13 shows the predicted curves using a stellar rotation synchronous with the orbital angular velocity whereby the spin or rotational period is synonymous with the orbital periods. Akin to the Moon keeping the same face toward Earth, this is the expected condition given ample evolution of any close binary system, because tidal effects yield this motion as the lowest energy configuration, as is the circular orbit arrangement compared with elliptical orbits.

Although Hilditch (2005) found rotational velocities 86% of the synchronous value more agreeable with his modeling, the scatter in our radial velocities could not discriminate this difference: our modeling can only specify within a $\pm$10% uncertainty for the synchronous rotational angular velocity of $2\pi/T_{period}$ with T_{period} = 2.05102655 days; therefore, we have less than a 2 SD discrepancy with Hilditch. Figure 13 shows good agreement with our radial velocities, even for the primary component near its eclipse where the influence of stellar rotation is evident; the Doppler-shift associated with either binary component is normally integrated across the stellar atmosphere, but this is restricted when an atmosphere is eclipsed.

Figure 12a illustrates the enhancement to the red shift of the primary star when its blue-shifted rotational side is eclipsed;

conversely, Fig. 12b illustrates the enhancement to the blue shift as the primary star emerges from this eclipse. Although the modeling predicts comparable rotational influence for the secondary component, we could not resolve this component in our H-alpha profiles near the secondary eclipse.

This rotational influence has been observed in many eclipsing binaries since the explanation first given by Rossiter (1924), and was evident in the radial velocities for 68Her reported by Smith (1945: fig. 1) – though he was limited by the capability of light-curve models at that time. Although three decades later Kovachev and Seggewiss (1975) found the Rossiter effect "less noticeable" in their radial velocities, we can confirm its substantial contribution.

ACKNOWLEDGEMENTS

We are thankful for the assistance of Professor John Waldmeir and Valorie Woerdehoff, and for the funding provided by the Alliant Energy Foundation, the Verizon Foundation, and the Dubuque Racing Association.

LITERATURE CITED

BERRY, R. and J. BURNELL. 2005. The handbook of astronomical image processing. Willmann-Bell, Richmond, Virginia.

BRADSTREET, D. H. 2005. Fundamentals of solving eclipsing binary light curves using Binary Maker 3. Pages. 23–37. *In*: B. Warner, D. Mais, D. Kenyon, and J. Foote (eds.). Proceedings for the 24th Annual Conference of the Society for Astronomical Science; 2005 May 25–26. Soc Astronom Sci, Inc., Big Bear Lake, California. [Rancho Cucamonga, California].

CARROLL, B. W. and D. A. OSTLIE. 2007. An introduction to modern astrophysics. 2nd edition. Pearson Addison-Wesley, San Francisco, California.

EASTMAN KODAK. 2000. Enhanced response full-frame CCD image sensor with anti-blooming protection: performance specification. Eastman Kodak Co., Rochester, New York. Accessed 30 April 2013 from http://www.digchip.com/datasheets/parts/datasheet/596/KAF-0401LE-pdf.php.

HENDEN, A. A. and R. H. KAITCHUCK. 1982. Astronomical photometry. Van Nostrand Reinhold, New York.

HILDITCH, R. W. 2005. Astrophysical parameters for the eclipsing binary u Herculis. The Observatory 125:72–81.

HOLMES, A. 2009. Operating instructions for the Santa Barbara Instrument Group self-guided spectrograph and spectra analysis software. Santa Barbara Instrument Group, Santa Barbara, California. Accessed 30 June 2015 from http://www.sbig.com/site/assets/files/18249/spectrograph__sgs5_.pdf.

KALLRATH, J. and E. F. MILONE. 2009. Eclipsing binary stars: modeling and analysis. Springer-Verlag, New York.

KOLBAS, V., A. DERVISOGLU, K. PAVLOVSKI, and J. SOUTHWORTH. 2014. Tracing CNO exposed layers in the Algol-type binary system u Her. Monthly Notices of the Royal Astronomical Society 444:3118–3129.

KOVACHEV, B. J. and M. REINHARDT. 1975. Spectroscopic evidence for extra-stellar matter in u Her. Acta Astronomica 25 (2):133–151.

KOVACHEV, B. J. and W. SEGGEWISS. 1975. A new spectroscopic orbit of the eclipsing binary 68u Her. Astronomy and Astrophysics, Supplement Series 19:395–402.

KRAMIDA, A., Y. RALCHENKO, J. READER, and NIST ASD Team. 2014. NIST Atomic Spectra Database. National Institute of Standards and Technology, Gaithersburg, Maryland. Accessed 30 March 2015 from http://www.nist.gov/pml/data/asd.cfm.

KREINER, J. M. 2004. Up-to-date linear elements of eclipsing binaries. Acta Astronomica 54:207–210.

MUNARI, U. and S. MORETTI. 2012. Characterizing the photometric response of the ANS collaboration monitoring program. Baltic Astronomy 21:22–31.

OLSON, E. C. 1968. Spectral classification and surface gravities for some bright eclipsing binaries. Astrophysical Journal 153:187–194.

PROVOOST, P. 1980. Interpretation of new BVR lightcurves of u Herculis. Astronomy & Astrophysics 81:17–24.

ROSSITER, R. A. 1924. On the detection of an effect of rotation during eclipse in the velocity of the brighter component of beta Lyrae, and on the constancy of the velocity of this system. Astrophysical Journal 60:15–21.

ROVITHIS-LIVANIOU, H. and P. E. ROVITHIS. 1985. Analysis of light curves of the eclipsing binary u Herculis. Astronomy and Astrophysics, Supplement Series 60(1–2):71–74.

SANTA BARBARA INSTRUMENT GROUP. Operating manual: CCD camera models ST-7E, ST-8E, ST-9E, ST-10E, and ST-1001E. Santa Barbara Instrument Group, Santa Barbara, California. Accessed 27 September 2015 from http://www.sbig.com/site/assets/files/18222/st78910man.pdf.

SMITH, B. 1945. A spectrographic study of 68 u Herculis. Astrophys Journal 102:500–510.

SODERHJELM S. 1978. MR Cyg and u Her: two similar eclipsing binaries. Astrophysical Journal 66:161–168.

SPECTROPHOTOMETRIC STANDARD STARS. European Southern Observatory, Munich, Germany. Accessed 31 May 2013 from http://www.eso.org/sci/observing/tools/standards/spectra/hr7001.html.

STERNE, T. E. 1941. Notes on binary stars: V. The determination by least-squares of the elements of spectroscopic binaries. Proceedings of the National Academy of Sciences 27(3):175–181.

VAN DER VEEN, W. E. C. J. 1985. Interpretation of new narrow band light curves of the eclipsing binary u Her. Astronomy & Astrophysics 145(2):380–386.